Simulating impacts of real-world wind farms on land surface temperature using the WRF model: physical mechanisms

Geng Xia[1] · Liming Zhou[1] · Justin R. Minder[1] · Robert G. Fovell[1] · Pedro A. Jimenez[2]

Abstract

A recent study shows that the current wind turbine parameterization in the weather research and forecasting (WRF) model can generally reproduce the satellite observed nighttime warming signal over wind farm (WF) regions over west central Texas, but also tends to produce a cooling effect in the WF downwind regions. The present study conducts a series of WRF simulations to further this research by addressing two fundamental questions: (i) what is the 3-D structure of simulated near-surface temperatures within and around WFs? (ii) what are the main physical mechanisms responsible for the simulated WF-induced temperature changes? Our results indicate that the WF-induced temperature changes are not only restricted to the surface but also can extend vertically to the hub-height level and horizontally in the downwind direction. The WF-induced change in sensible heat flux is the dominant factor for the simulated temperature changes at the surface, for both the warming signals over the WF region and the cooling signals behind it. Further diagnosis shows that the turbulent component of the wind turbine parameterization is responsible for the surface warming signal by enhancing vertical mixing while the momentum sink component is responsible for the surface cooling signal by enhancing near-surface thermal stratification. By analyzing the energy budget, we find two important physical processes that are critical to explain the simulated WF impacts on temperature: (i) vertical divergence of heat flux as parameterized in the planetary boundary layer scheme and (ii) resolved-scale 3-D temperature advection.

1 Introduction

Continued growth in renewable wind energy has motivated investigation into detecting, attributing and quantifying wind farm (WF) impacts on near-surface microclimate. Such impacts, if large enough, may have important implications for the sustainability and growth of renewable wind energy as well as agriculture in the U.S., especially over the Great Plains (Armstrong et al. 2014, 2016; Tang et al. 2017; Xia and Zhou 2017a). Using in situ observations, Baidya and Traiteur (2010) found that a WF at San Gorgonio, California,

tended to increase the near-surface air temperature when the boundary layer was stably stratified at nighttime. Using satellite derived land surface temperature (LST) data from the Moderate Resolution Imaging Spectroradimeter (MODIS), Zhou et al. (2012, 2013a, b) observed a significant surface warming signal over several large WFs in west-central Texas at nighttime but not at daytime. Since then, both local and regional WF impacts on near-surface temperature have been observed using satellite data over other large WFs (Harris et al. 2014; Slawsky et al. 2015; Chang et al. 2016; Xia et al. 2016) and using in situ measurements in field campaigns (Smith et al. 2013; Rajewski et al. 2013, 2014). However, the possible physical mechanisms linking operating WFs and detected microclimate impacts have only been proposed and not yet fully confirmed by observations (Xia et al. 2016; Rajewski et al. 2016).

Due to limited availability of field data and relatively inexpensive computational resources, mesoscale modeling has become a primary approach to understand WF impacts at regional scales. Fitch et al. (2012) developed a sophisticated wind turbine (WT) parameterization for the Weather Research and Forecasting (WRF) model (Skamarock and

✉ Geng Xia
  gxia@albany.edu

[1] Department of Atmospheric and Environmental Sciences, University at Albany, State University of New York, 1400 Washington Avenue, Albany, NY 12222, USA

[2] Research Applications Laboratory, NCAR, Boulder, CO, USA

Klemp 2008) and examined the influences of WFs throughout a diurnal cycle in an idealized simulation (Fitch et al. 2013). They found a near-surface warming of 0.5 K over the WF region during the night and morning transition and attributed this warming signal to the negative surface sensible heat flux change. Using the same WT parameterization, Xia et al. (2017b) conducted a series of real-world WF simulations using the WRF model driven by realistic initial and boundary conditions and compared the simulated WF impact on LST with MODIS observations. The simulations were performed over west-central Texas for the month of July for a total of 7 years (2003–2004 and 2010–2014). The results indicate that the simulated WF-induced LST warming signals agree well with the satellite observations in terms of their spatial coupling with the WF layout although the simulated areal mean warming magnitude is about 30% smaller than that detected from MODIS. However, the model tends to produce a prevailing surface cooling signal over the downwind region, which has not been confirmed by any previous field campaigns or satellite observations, and thus may indicate a deficiency in the WT parameterization.

The work of Xia et al. (2017b) represents an improvement upon an earlier effort by Cervarich et al. (2013) to simulate real-world WF impacts on LST changes. However, it does not address fundamental scientific questions such as: (i) what is the 3-D structure of simulated near-surface temperatures within and around WFs, and (ii) what are the main physical mechanisms responsible for the simulated WF-induced temperature changes? To elucidate potential physical processes involved, further inquiries into the impacts of WFs are definitely needed with numerical experiments. Therefore, the purpose of this paper is to further the work of Xia et al. (2017b) to answer these fundamental questions from the modeling perspective.

The rest of this paper is structured as follows. Section 2 describes the experiment design and methodology. Section 3 explains and discusses the simulation results. Section 4 addresses the uncertainties associated with the model simulations. Section 5 presents our conclusions.

2 Experiment design and methodology

2.1 Experiment design

The aim of the present study is to further the work of Xia et al. (2017b) to explicitly address the near-surface temperature responses to operating WFs and uncover the associated possible physical mechanisms. To do this, we conduct simulations using the WRF (v3.6.1) model and a domain configuration and a physical parameterizations suite that are identical to Xia et al. (2017b). The reader can refer to that paper for full details. Briefly, a two-way
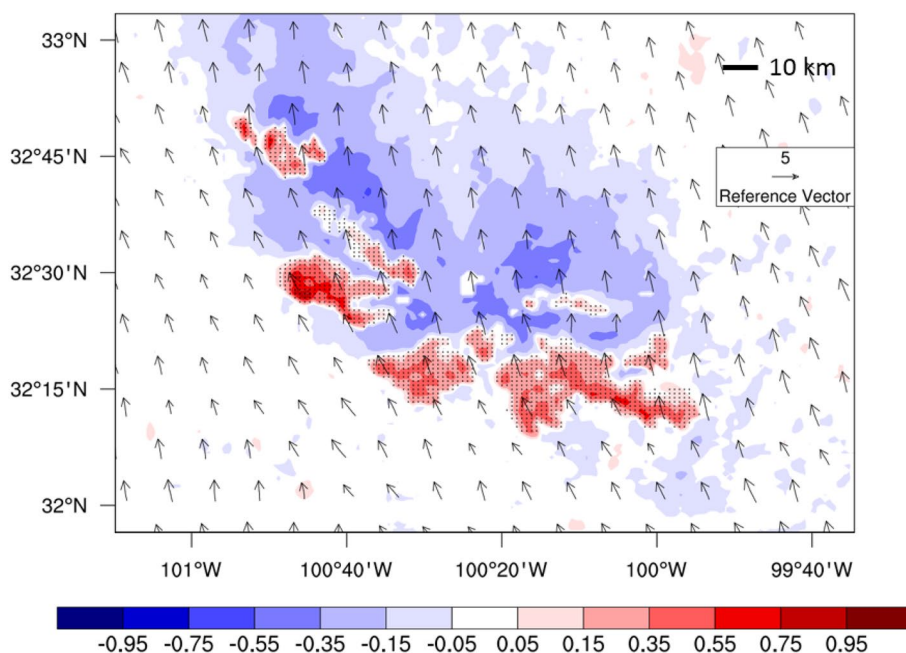
nested grid configuration is employed in order to ensure minimal interactions with lateral boundaries. There are three domains with the horizontal grid spacing of 25 km, 5 km and 1 km, respectively. In the vertical, there are 39 levels, ten of which are within the lowest 200 m above the surface. The Mellor–Yamada Nakanishi–Niino planetary boundary layer (PBL) scheme (MYNN, Nakanishi and Niino 2009) is used because it is the only PBL scheme that is compatible with the current WT parameterization.

To conserve computer resources, we only conduct three-day reinitialized (3Day) simulations for the month of July in 2011. Similar to Xia et al. (2017b), the 3Day simulations are initialized at 0000 UTC and run for 72 h, providing 15 short segments (each with one day overlap) to cover the entire month. For instance, the first 3-day simulation starts on June 30th and ends on July 2nd. The first day is treated as spin-up and only the last 2 days are retained for analysis. The rest of the 3Day simulations are conducted in a similar manner.

We choose the month of July 2011 because every night during this month in our simulations is considered to be cloud-free (Xia et al. 2017b). We calculate the cloud liquid water path from the WRF default output and use it as an indicator to quantify cloud cover in the domain. If a night has cloud cover exceeding a threshold value of 0.02 kg m^{-2} for more than 15% of the entire WF and its immediate vicinity (~5 km around the WF) from 2200 to 0200 LT, we consider that night as a cloudy night (Xia et al. 2017b). This is a critical criterion to consider as our simulations were validated against MODIS observations under clear sky conditions. Figure 1 shows spatial patterns of the simulated LST changes with and without the WT parameterization averaged between 22:00 LT to 02:00 LT for July 2011. Evidently, there is a clear LST warming signal over the wind farm region and a distinct cooling signal over the downwind region (immediately behind the wind farm region). Such features resemble the previous multi-year simulations of Xia et al. (2017b).

The WT parameterization in the WRF model was developed by Fitch et al. (2012). It represents the effect of a WT by imposing a momentum sink term and a turbulence kinetic energy (TKE) source term onto the model layer containing the WT. For uniformity, all WTs use the 2.0 MW WT coefficients (Adams and Keith 2013) and are assumed to have 100 m hub-height, 100 m rotor diameter, 3 m s^{-1} cut-in speed and 25 m s^{-1} cut-out speed. The cut-in and cut-out speeds bracket the range at which a typical WT operates. If multiple turbines are located within a single grid cell, the changes in kinetic energy and TKE are multiplied by the number of turbines within the cell and averaged over the cell. The turbine blades are assumed to be oriented perpendicular to the wind as this is how turbines normally operate. Previous work has indicated that this parameterization can

Fig. 1 Spatial patterns of the nighttime LST (°C) differences between simulations with and without the wind turbine parameterization for July 2011. The simulated nighttime LST changes are averaged from hourly model output between 22:00 LT and 02:00 LT. Symbols represent all the grids (917) containing at least one real wind turbine. The 10-m winds from the CTRL simulation are shown as vectors

qualitatively reproduce the turbine-flow interactions under different atmospheric conditions (Jimenez et al. 2015).

We define two regions, the wind farm region (WFR) and the downwind non-wind farm region (NWFR) in the 1 km nest, to quantify the simulated WF impact on temperature. Figure 2a shows the realistic WF configuration as employed in Xia et al. (2017b), where the WFR consists of 917 grid cells containing real-world WTs according to their actual geographical locations and the NWFR has 940 grid cells within 1–10 km north of the WFR that do not contain any WTs. Note that the prevailing wind direction over the study region is from the south and each grid in the WFR may contain one or more WTs.

To better illustrate the spatiotemporal evolution of the simulated temperature change, an idealized WF configuration is also constructed as shown in Fig. 2b, where we defined an idealized WFR (20 × 20 grid cells, with one turbine for each grid) over the center of the domain. Because of the simple geometry in this configuration, we can easily compute the vertical cross sections over the WFR and its wake while minimizing the complication associated with the irregular WF shape in the realistic WF configuration.

To investigate how the two individual components (e.g., TKE and momentum) of the WT parameterization behave and contribute to the simulated temperature changes, four experiments are performed for each WF configuration: one without the WT parameterization (denoted CTR), one with the full WT parameterization active (denoted ALL), one with only the momentum sink component of the WT parameterization active (denoted MOM), and with only the TKE component of the WT parameterization active (denoted TUR). The contribution of each component is assessed by
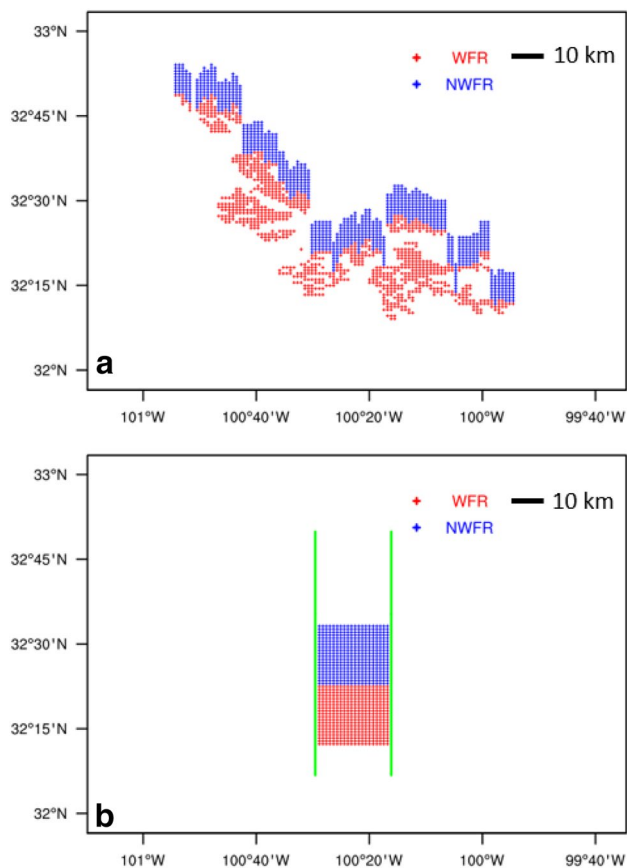

Fig. 2 The geographical location of wind farm region (WFR) and downwind non-wind farm region (NWFR) for the two WF configurations at 1 km grid spacing: **a** the realistic WF configuration; **b** a hypothetical WF configuration

taking the difference between the control (CTR) and the experiment simulations (ALL, MOM, and TUR).

2.2 Methodology

2.2.1 Analysis of WF-induced changes in surface energy budget

The changes in LST are controlled primarily by the surface energy budget, which is a radiation and heat balance, typically applied to the interface between the atmosphere and the surface of the earth. The classical formation is

$$\mathrm{SR} + \mathrm{LR}(T_g) + \mathrm{SH}(T_g) + \mathrm{LH}(T_g) + \mathrm{G}(T_g) = 0, \qquad (1)$$

where SR is the net solar radiation, LR is the net longwave radiation, SH is the sensible heat flux, LH is the latent heat flux and G is the ground heat flux. Note that SR, LR, SH and LH are defined as positive toward the atmosphere and G is defined as positive toward the soil. LR, SH, LH and G depend on the ground temperature, T_g. As our study region is a semi-arid system with very limited vegetation, T_g can be simply treated as an approximation to LST (Zhou et al. 2003a, b). At nighttime, SR is zero and thus LST is determined by the energy budget between LR and the three non-radiative surface heat fluxes. Perturbations from the WT parameterization will have an indirect impact on the surface heat fluxes via their contributions to PBL mixing (Sect. 2.2.2), which will then alter the LST. Therefore, by examining the relative changes (e.g., sign and magnitude) of the surface heat fluxes, we can determine the dominant factors that are responsible for the simulated LST changes. We use the Student's t test to quantify the statistical significance of the areal mean changes of each surface variable. A t value exceeding the 95% confidence level (i.e., $p < 0.05$, n = 30) is considered to be statistically significant.

2.2.2 Possible physical processes for WF-induced temperature changes

The change in potential temperature in the WRF model can be written as

$$\frac{\partial \theta}{\partial t} + (\nabla \cdot V\theta) = F_\theta, \qquad (2)$$

where θ is the potential temperature, V is the three-dimensional wind speed and F_θ represents forcing terms arising from model physics, turbulent mixing, spherical projections and the earth's rotation. If we further break down F_θ with respective to different processes, Eq. (2) can be expressed as

$$\mathrm{TT} = \mathrm{TT\_ADV} + \mathrm{TT\_PBL} + \mathrm{TT\_RAD} + \mathrm{TT\_DIF} + \mathrm{TT\_RES}, \qquad (3)$$

where TT stands for the overall temperature tendency, TT_ADV is the temperature tendency induced by the advection process, TT_PBL is induced by the PBL scheme, TT_RAD is induced by the radiation scheme, TT_DIF is induced by the diffusion process and TT_RES is induced by the other physical and dynamical processes that are simulated in the WRF model.

As mentioned in Sect. 2.1, the main effect of the WT parameterization is to impose a momentum sink term as well as a TKE source term over the rotor area. Although the parameterization does not directly modify the mean temperature within a grid cell, it can indirectly affect temperature through perturbing the near-surface turbulent flux terms in the PBL scheme. Thus the simulated temperature changes induced by the WT parameterization must be primarily associated with the temperature changes induced by the PBL scheme.

In the WRF model, the PBL scheme is responsible for vertical subgrid-scale fluxes due to eddy transports. It determines the flux profiles within the well-mixed boundary layer and the stable layer, and thus provides atmospheric tendencies of temperature and momentum in the entire atmospheric column. Therefore, the temperature tendency induced by the PBL scheme (TT_PBL) is determined by the vertical divergence of sub-grid turbulent heat $w'\theta'$, as indicated in Eq. (4).

$$\mathrm{TT\_PBL} = -\frac{\partial w'\theta'}{\partial z}, \qquad (4)$$

where θ' is the turbulent component of the potential temperature, w' is the turbulent component of the vertical velocity and the angle bracket $< >$ is the averaging operator. In this study, we output both TT_PBL and $w'\theta'$ directly from the WRF model to quantify how the turbulent heat flux responds to perturbations caused by the WT parameterization in the PBL scheme.

Other than the vertical divergence of the turbulent heat flux, another physical process that might be critical to the simulated temperature changes is the resolved-scale 3-D temperature advection (referred to as TT_ADV hereafter) computed in the WRF model dynamic core. The corresponding equation is shown below:

$$\mathrm{TT\_ADV} = \mathrm{U}\frac{d\theta}{dx} + \mathrm{V}\frac{d\theta}{dy} + \mathrm{W}\frac{d\theta}{dz}. \qquad (5)$$

As shown in Fig. 1, the spatial pattern of the cooling signal follows along with the 10 m height wind vector, suggesting that the surface cooling anomalies are advected downwind. Therefore, we obtain TT_ADV directly from the WRF model to assess its relative contribution to the simulated temperature changes. Note that TT_ADV is calculated during every Runge–Kutta

sub-step (Skamarock and Klemp 2008). Thus, we save TT_ADV from each sub-step and compute the mean value for further analysis.

Similar to Xia et al. (2017b), we will only discuss the results during the nighttime hours because the simulated WF impacts during daytime are negligible.

3 Results and discussion

3.1 WF-induced changes in surface energy budget

Figure 3 shows spatial patterns of the nighttime changes in LST, LR, SH, LH and GH fluxes from the three experiments (ALL, MOM, TUR). Overall, the WT parameterization produces LST warming over the WFR and LST cooling over the downwind region (Fig. 3a). However, it is clear that the TKE
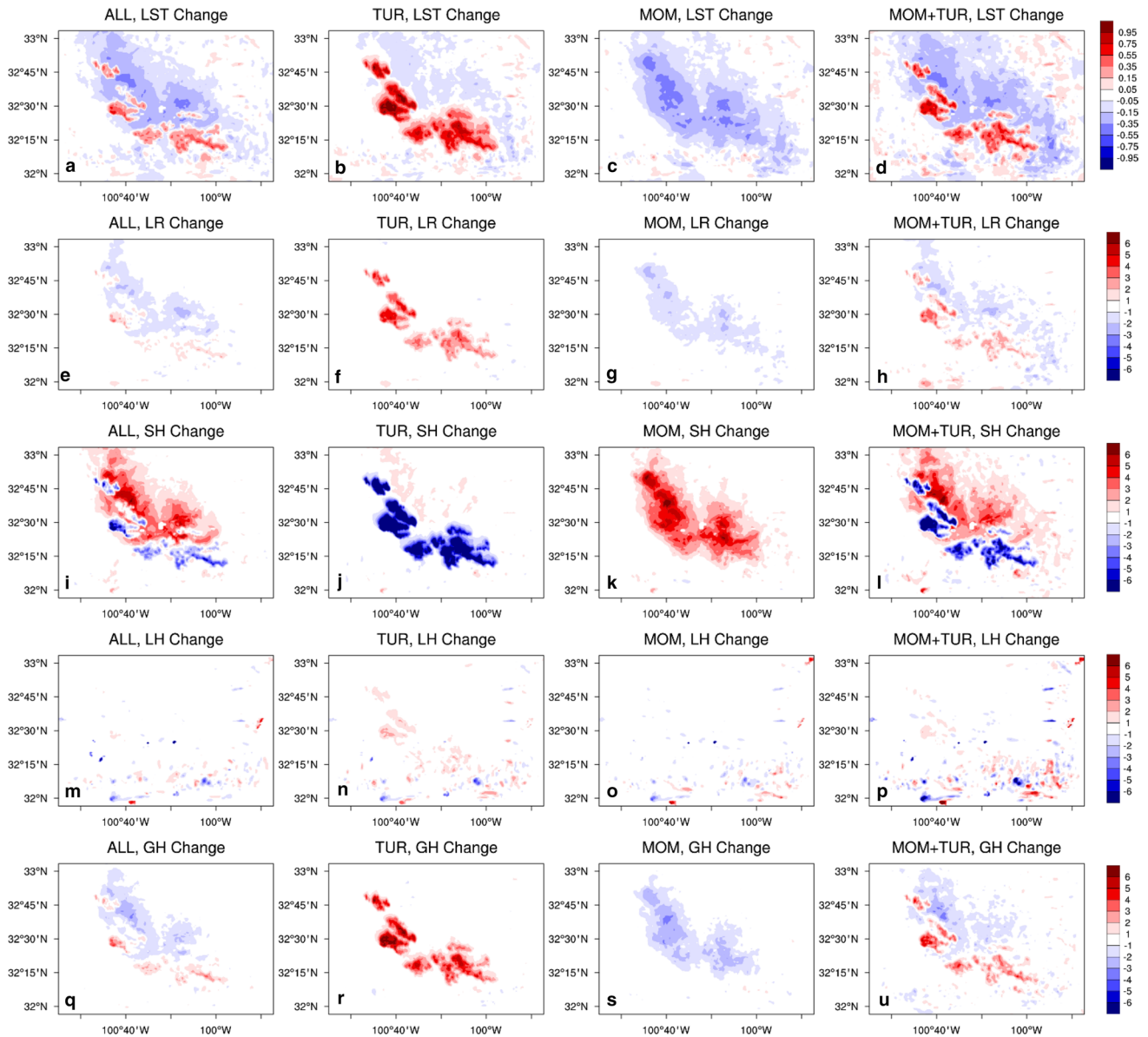
Fig. 3 Spatial patterns of the nighttime LST (°C), LR flux (W m^{-2}), SH flux (W m^{-2}), LH flux (W m^{-2}) and GH flux (W m^{-2}) differences between simulations with and without the wind turbine parameterization for July 2011: **a–d** LST changes from the ALL, TUR, MOM and TUR + MOM experiments respectively; **e–h** similar to **a–d** but for LR flux changes; **i–l** similar to **a–d** but for SH flux changes; **m–p** similar to **a–d** but for LH flux changes; **q–u** similar to **a–d** but for GH flux changes. The simulated changes are averaged from hourly model output between 22:00 LT and 02:00 LT

Table 1 Areal mean changes and standard deviation (in parenthesis) in LST (ΔLST, °C), net longwave radiation (ΔLR, W m^{-2}), SH flux (ΔSH, W m^{-2}), LH flux (ΔLH, W m^{-2}) and GH flux (ΔGH, W m^{-2}) over the WFR from the ALL, TUR and MOM experiments

	ALL	TUR	MOM	TUR+MOM
ΔLST	**0.22** (0.10)	**0.63** (0.24)	**− 0.21** (0.14)	**0.41** (0.16)
ΔLR	**0.68** (0.47)	**2.70** (1.18)	**− 1.12** (0.54)	**1.57** (0.91)
ΔSH	**− 1.83** (1.14)	**− 7.30** (3.00)	**3.08** (1.61)	**− 4.22** (1.96)
ΔLH	**0.27** (0.27)	**1.01** (0.44)	**− 0.39** (0.27)	**0.61** (0.32)
ΔGH	**0.87** (0.58)	**3.60** (1.53)	**− 1.56** (0.92)	**2.03** (1.00)

Areal mean changes in bold are statistically significant at the 5% level

The geographical locations of the WFR are defined in Fig. 2a

Table 2 Similar to Table 1 but over the NWFR

	ALL	TUR	MOM	TUR+MOM
ΔLST	**− 0.16** (0.12)	**0.17** (0.08)	**− 0.27** (0.16)	**− 0.10** (0.13)
ΔLR	**− 1.06** (0.58)	**0.56** (0.43)	**− 1.38** (0.68)	**− 0.83** (0.75)
ΔSH	**2.31** (1.68)	**− 2.03** (0.96)	**3.47** (2.21)	**1.44** (1.97)
ΔLH	**− 0.36** (0.28)	**0.31** (0.20)	**− 0.54** (0.44)	− 0.23 (0.50)
ΔGH	**− 0.97** (0.98)	**1.14** (0.61)	**− 1.60** (1.30)	− 0.46 (1.26)

The geographical locations of the NWFR are defined in Fig. 2a

component of the WT parameterization (Fig. 3b) is responsible for the surface warming signal whereas the momentum component (Fig. 3c) is responsible for the surface cooling signal. The changes in near-surface air temperature (2 m) are also examined but not shown because they share almost identical changes both in spatial pattern and magnitude as LST, indicating little differences in the WF impacts on these two variables, at least from the modeling perspective.

The change in surface energy budget is also documented. The positive (negative) LR fluxes from Fig. 3e–h resemble the LST warming (cooling) with respect to the spatial patterns and magnitude, indicating more (less) outgoing thermal emission due to the WF-induced surface warming (cooling). Similarly, the negative (positive) SH fluxes from Fig. 3i–l indicate more heat is transferred from the atmosphere (ground) to the ground (atmosphere) and the positive (negative) LH fluxes from Fig. 3m–p indicate more (less) turbine-enhanced evaporation. The positive (negative) GH fluxes from Fig. 3q–u indicate more (less) heat storage in the soil.

To quantify the WF impacts, Tables 1 and 2 list the areal mean changes and standard deviation (SD, in parenthesis) in temperature and surface fluxes over the WFR and NWFR, respectively. Note that the areal mean changes in bold are statistically significant at the 5% level (p < 0.05, n = 30). Again, we note that the TKE component is responsible for the surface warming and the momentum component is responsible for the surface cooling. It is interesting

to see that the simulated warming signal is mostly confined to the WFR (0.63 °C) as opposed to the NWFR (0.17 °C) in the TUR experiment whereas the cooling signal is similar between the NWFR and WFR in the MOM experiment. This might suggest that the process of temperature advection plays a key role in the MOM experiment (see more results in Sect. 3.4). Notice that the SD of the simulated LST changes is quite large in all three simulations. However, the warming and cooling signals from the TUR and MOM are consistent throughout the 30-day period (see more discussion in Sect. 4).

In addition, the changes of SH flux (− 7.30 to 3.47 W m^{-2}) are significantly greater than those of GH flux (− 1.60 to 3.60 W m^{-2}) and LH flux (− 0.39 to 1.01 W m^{-2}) respectively, suggesting that SH flux is the most dominant forcing responsible for the simulated temperature changes at the surface. In particular, the negative (positive) SH flux is primarily balanced by other positive (negative) fluxes, further suggesting that the WF-induced vertical heat transport via SH is the primary energy source for the changes in LST and energy budget. This result agrees well with another recent WF validation study (Lee and Lundquist 2017).

Interestingly, if we just simply add the changes of each flux (LST, LR, SH, LH and GH) from the TUR and MOM experiments together, the combined results (Fig. 3d, h, l, p, u) are unanimously larger in magnitude than the results from the ALL over the WFR (Tables 1, 2), but weaker over the NWFR. In addition, all the areal mean changes are statistically significant, except for ΔLH and ΔGH when the results from the TUR and MOM are linearly combined. These suggest that there are non-linear interactions between the momentum and TKE terms in the MYNN PBL scheme, which should not be a surprise because these two processes are fully coupled. In other words, introducing perturbations to the momentum field will influence the TKE field and vice-versa. However, this adds complexity to discussions of the relative contribution of each component to the simulated temperature changes because these two effects cannot be easily separated (Sun et al. 2018).

If we calculate the net simulated WF impacts on LST by combing ΔLST over the two model domains of WFR and NWFR (Fig. 2a), we find that there is a small net surface warming (0.06 °C), suggesting that the warming in WFR and cooling in NWFR mostly average out in the spatial mean.

A similar analysis is conducted using the idealized WF configuration (Figure S1, Table S1 and Table S2). Consistent with the previous conclusions, the change in SH flux is responsible for the simulated temperature change at the surface and the TKE (momentum) component of the WT parameterization produces the surface warming (cooling) signal.

3.2 Vertical profiles of WF-induced temperature changes

Figure 4a, b show the mean vertical profiles of the simulated temperature changes between 19:00 LT and 06:00 LT over the WFR and NWFR using the realistic WF configuration (Fig. 2a) from the ALL, TUR and MOM experiments. Note that we only examine the lowest 400 m above ground level (AGL) because the vertical resolution gets coarser as height increases and the magnitude of the temperature perturbations is small. Over the WFR, the near-surface warming signal (0.55 °C) is associated with the TKE source term while the near-surface cooling signal (− 0.19 °C) is associated with the momentum sink term. In addition, both terms contribute to the warming signal (0.15 °C) around the hub-height levels. Overall, the simulated warming signal is strongest at the surface (0.22 °C) and decreases with height. Above the maximum rotor height (150 m), both components contribute to the cooling signal (− 0.08 °C).

Over the NWFR, the profiles of WF-induced temperature changes from each experiment depict similar features as those from the WFR, such as the upper-level cooling (− 0.07 °C) and the hub-height warming (0.15 °C). However, the biggest difference is the reduced strength of the low-level heating (lowest 30 m AGL) associated with the TUR component, which allows the MOM component to dominate, resulting in a net surface cooling (− 0.13 °C). Similar results are found when using the idealized WF configuration (Figure S2), except that the magnitude is smaller due to fewer WTs.

To further understand the vertical structure of the simulated temperature changes, Fig. 5 shows the vertical cross sections of the simulated temperature changes over the idealized WF configuration (averaged between two green lines) from 19:00 LT to 06:00 LT from the ALL experiment. The

WFR is located between the two green lines at the bottom of each figure. Note that we do not show a similar analysis with the realistic WF configuration (Fig. 2a) because of the complicated WT layout. From 19:00 LT to 20:00 LT, there are negligible changes in temperature because the mixing from the daytime convective PBL is still dominant, as is evident from a time series of average PBL height over the simulation domain (Fig. 6). Note that the PBL height is determined by a TKE-based approach in the MYNN PBL scheme. However, as the PBL quickly transits from the daytime convective state into the nighttime stable state, the impacts of WTs on temperature begin to appear.

Starting from 21:00 LT, the surface warming signal occurs over the WFR while a cooling signal develops above the hub-height level and at the downwind edge of the WFR. At 22:00 LT, the surface warming and cooling signals strengthen. In addition, a secondary warming pattern develops around the hub-height levels and then connects with the surface. From 23:00 LT to 03:00 LT, most of the WF-induced changes, such as the surface warming/cooling signals, the secondary warming signal as well as the cooling above the hub-height level, extend and intensify both horizontally and vertically away from the WFR. In particular, a 0.1 °C surface cooling and a 0.15 °C secondary warming signals extend ~ 60 km into the downwind direction. This downwind extension of the simulated warming and cooling signals suggest the importance of temperature advection as the perturbation from the WT parameterization is only active over the WFR. From 04:00 LT to 06:00 LT, the simulated temperature changes start to weaken and disappear around 09:00 LT (Figure not shown). To our best knowledge, most of these detailed changes have not been reported or confirmed in any previous field campaigns or satellite observations.

Fig. 4 Areal mean vertical profiles of the simulated WF-induced temperature changes between 19:00 LT to 06:00 LT from the ALL, TUR and MOM experiments: **a** averaged over the WFR defined in Fig. 2a, **b** averaged over the NWFR defined in Fig. 2a. The purple lines indicate the rotor disk region
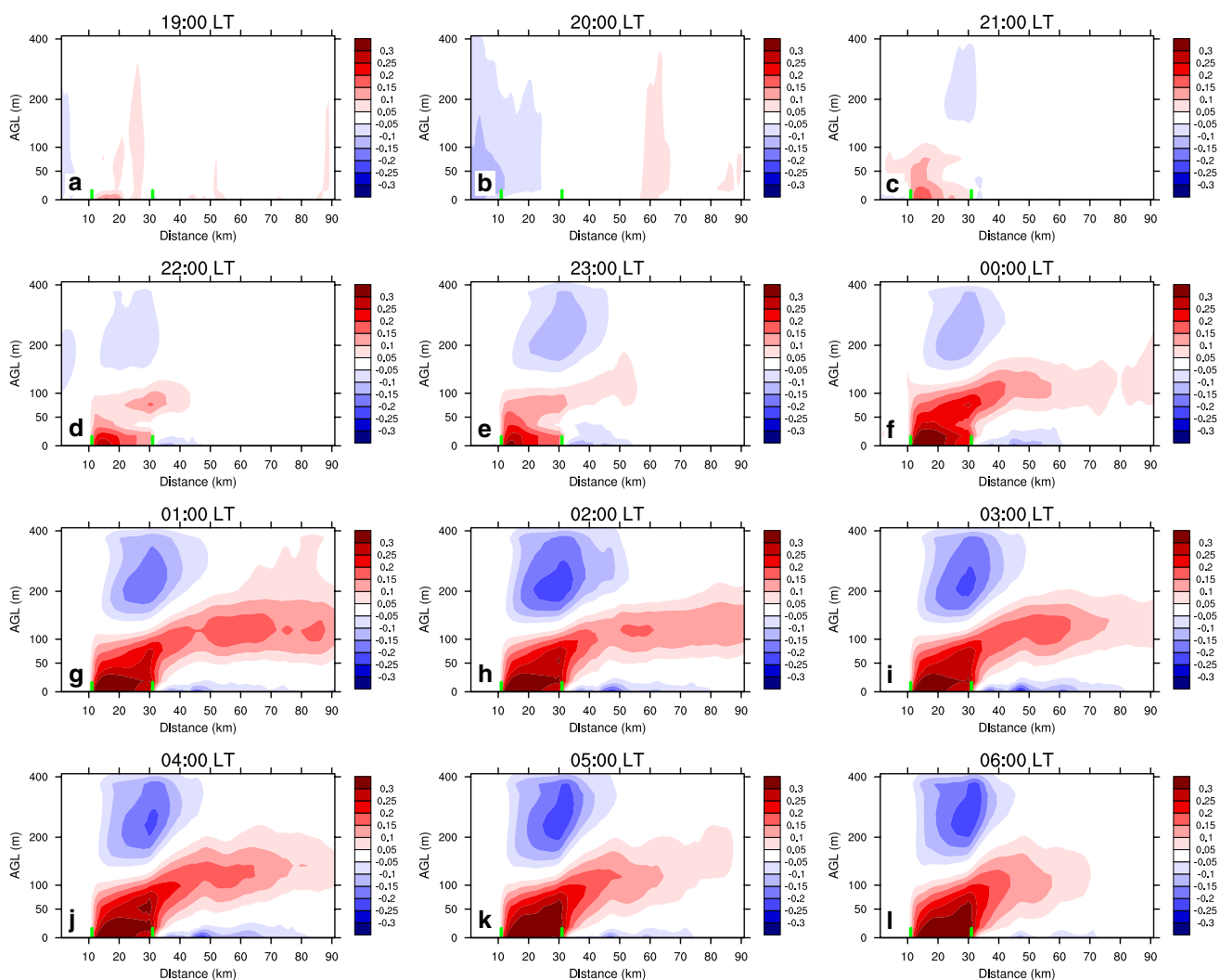
Fig. 5 Vertical cross sections (averaged between two green lines from Fig. 2b) of the simulated temperature differences (°C) between simulations with and without the wind turbine parameterization from 19:00 LT to 06:00 LT from the ALL experiment. The WFR is located between the two green lines (10–30 km) at the bottom of each figure

To illustrate the contributions from each individual component to the WF-induced temperature changes, Fig. 7 shows the same figure as Fig. 5 but from all three experiments (ALL, TUR and MOM) at 22:00 LT, 01:00 LT and 04:00 LT only. We choose these three time periods as they generally represent the start, mature and decay stages of the simulated temperature evolution at nighttime. Similar to what we have discussed previously, the warming over the WFR is associated with the TKE component (Fig. 7d–f) whereas the momentum sink component (Fig. 7g–i) is responsible for the warming around the hub-height levels as well as the near-surface cooling signal. In addition, both components contribute to the simulated cooling effect above the rotor area. Evidently, the simulated surface cooling (~ -0.1 °C) and the hub-height warming (~ 0.15 °C) can spread as far as ~ 60 km away from the WFR in the ALL experiment. This

downwind expansion feature, which highlights the importance of advection process, is mainly associated with the momentum sink component of the WT parameterization. Again, the combined temperature responses from the TUR and MOM experiments (Fig. 7j–l) are stronger than the responses from the ALL experiment (Fig. 7a–c), suggesting non-linear interactions between the momentum and TKE processes in the PBL scheme.

3.3 Contribution from turbulent heat flux to the temperature tendency

The current WT parameterization represents the effects of individual WTs on the atmosphere by imposing a momentum sink term and a TKE source term on the mean flow, which in turn can affect the mixing parameterized by the
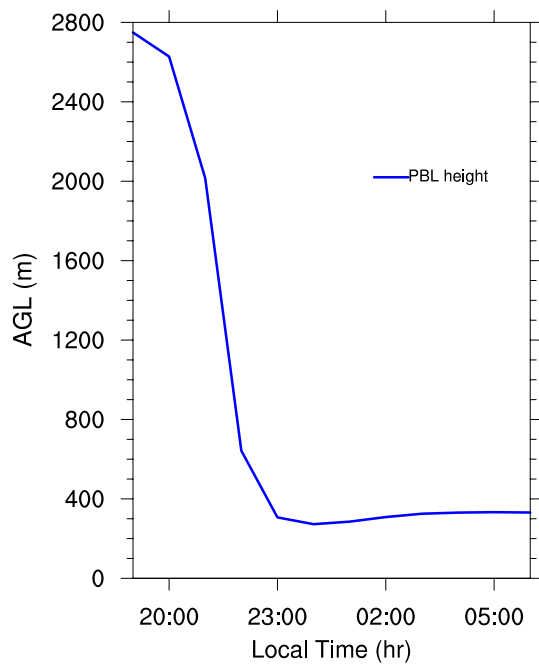
Fig. 6 Evolution of mean PBL height (m) over the simulation domain from 19:00 LT to 06:00 LT from the CTRL simulation

PBL scheme. Therefore, the simulated temperature changes have to be primarily associated with the changes in the vertical mixing from the PBL scheme.

Figure 8 demonstrates the nighttime evolution of the WF-induced changes in TT_PBL and $w'\theta'$averaged over the WFR (Fig. 8a, c, e) and NWFR (Fig. 8b, d, f) to highlight how the PBL scheme and the WT parameterization work together to create temperature perturbations over both the WF and downwind regions. Notice that the colored contour indicates the changes in TT_PBL whereas the green line indicates the changes in $w'\theta'$. For the remainder of the paper, we only show the results over the WFR and NWFR from the realistic WF configuration (Fig. 2a) unless stated otherwise. This is to avoid figure redundancy because the idealized WF configuration exhibits very similar results as discussed previously (Figures S1 and S2; Tables S1 and S2).

In both the ALL and TUR experiments, the nighttime evolution of TT_PBL over the WFR indicates warming below 100 m AGL and cooling above it. However, the MOM experiment indicates cooling below 40 m AGL and above 150 AGL while warming occurs around the hub-height levels. Over the NWFR, TT_PBL from all three experiments indicates cooling below 50 m AGL and warming around the hub-height levels (50–150 m). In the MOM experiment, negative TT_PBL prevails above 200 m AGL whereas positive TT_PBL dominates in the TUR experiment.

The relationship between $w'\theta'$and TT_PBL is demonstrated in Eq. (4). The negative vertical gradient of $w'\theta'$

determines the sign and magnitude of TT_PBL. For example, Fig. 8a shows the nighttime evolution of TT_PBL and $w'\theta'$ over the WFR from the ALL experiment. Evidently, the negative (downward) WF-induced heat flux persists through the night, which helps to explain the negative SH flux as well as the surface warming signal (Fig. 3). From the surface up to the zero (white colored) contour, the gradient of $w'\theta'$ is negative so TT_PBL is positive. Going further upward, the gradient of $w'\theta'$is positive and therefore TT_PBL is negative. Thus, the relationship between $w'\theta'$ and TT_PBL is well established and physically reasonable. The same relationship is also valid for the other panels in Fig. 8 as well.

Near the surface, the TKE effect of the WT parameterization produces downward (negative) heat flux whereas the momentum effect produces upward (positive) heat flux. The differences in the changes of heat flux between the TKE and momentum components explain why the surface warms in the TUR experiment but cools in the MOM experiment (Fig. 3). When additional TKE is added over the rotor layers (TUR experiment), it induces additional vertical mixing, which brings down potentially warmer air from aloft and thus, increases the near-surface temperature. Note that this added TKE is quickly dissipated as it is advected downwind of the WFR, such that the warming in the TUR experiment is mostly confined closely to the WFR. However, it is not as intuitive to understand why the surface cools in the MOM experiment.

Figure 9 shows the nighttime evolution of changes in TKE, vertical gradient of potential temperature and $w'\theta'$ averaged over the WFR and NWFR between the MOM and CTRL runs. Evidently, TKE is reduced below the hub-height level but is increased above (Fig. 9a, b) over the WFR. These changes in TKE are mostly associated with the changes in wind shear as shown in Fig. 10a. Wind shear decreases below the hub-height, leading to reduced TKE production, but increases above, leading to increased TKE production. Over the NWFR, increased TKE above the hub-height level is significantly reduced because of dissipation (Figure not shown) but the TKE reduction near the surface is enhanced. As the change in wind shear is less prominent over the NWFR (Fig. 10b), the majority of the reduced TKE must be advected from the WFR. Note that the horizontal advection of TKE is employed in the simulations. Nevertheless, the reduction in mixing over both the WFR and NWFR from the MOM experiment strengthens the near-surface thermal stratification. As shown in Fig. 9c, d, the vertical gradient of potential temperature (dθ/dz) increases significantly near the surface over both the WFR and NWFR, producing a less favorable background environment for turbulent heat fluxes (Fig. 9e, f) to transport warmer air from aloft to the surface.
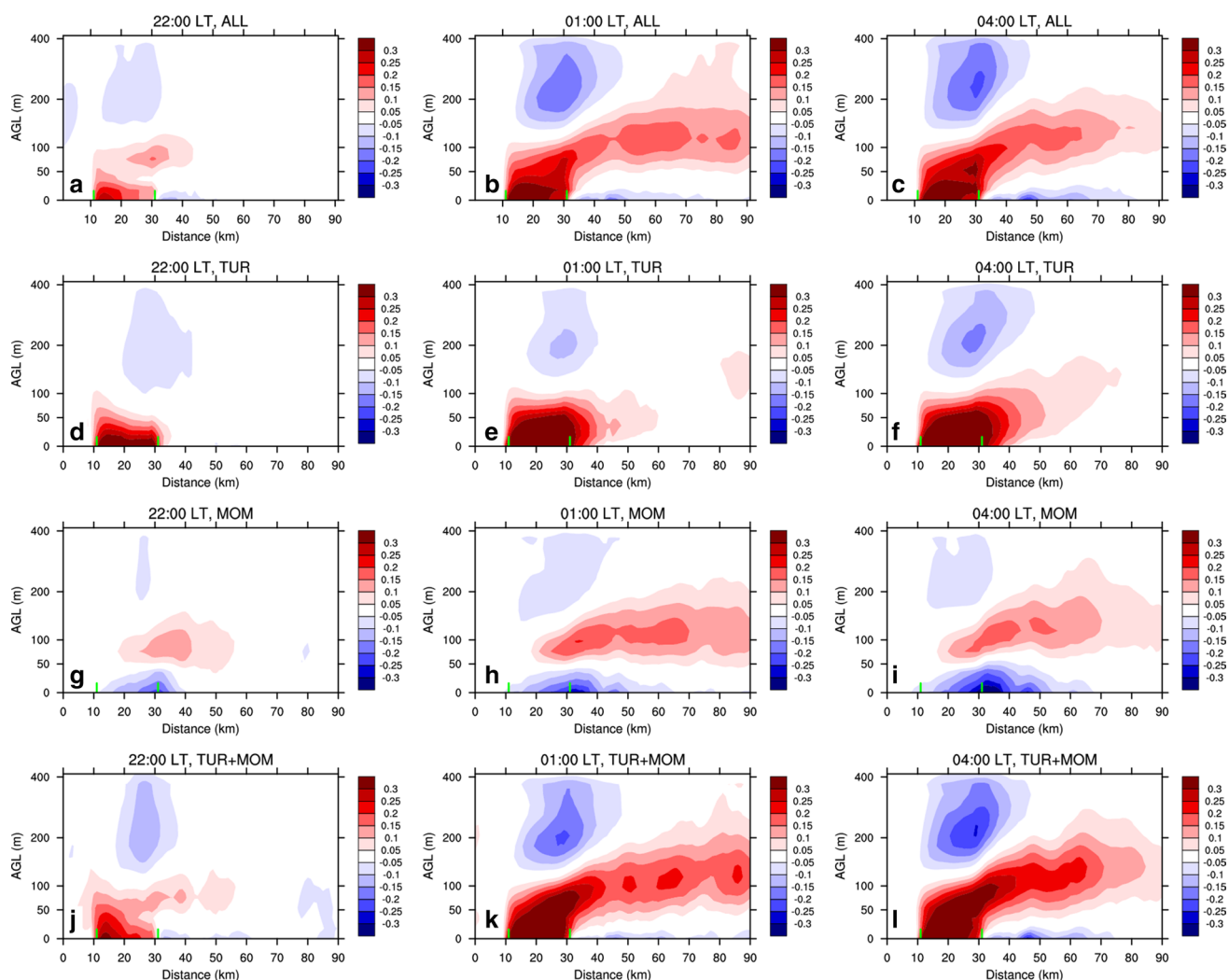
Fig. 7 Vertical cross sections (averaged between two green lines from Fig. 2b) of the simulated temperature differences (°C) between simulations with and without the wind turbine parameterization at 22:00 LT, 01:00 LT and 04:00 LT: **a–c** the ALL experiment; **d–f** similar to **a–c** but from the TUR experiment; **g–i** similar to **a–c** but from the MOM experiment; **j–l** similar to **a–c** but from the TUR+MOM experiments. The WFR is located between the two green lines (10–30 km) at the bottom of each figure

3.4 Contribution from other processes

In the previous section, we identified the vertical divergence of turbulence heat flux is an important physical mechanism responsible for the simulated temperature changes. Another relevant physical mechanism could be 3-D temperature advection as there is a prominent downwind evolution of the simulated temperature changes in the previous figures (Figs. 1, 5, 7). If this is the case, the evolution of the changes in TT_PBL and TT_ADV should be well coupled with the simulated temperatures changes. Furthermore, the combined effects from these two processes (TT_COMBINE) should also be able to explain the majority, if not all, of the WF-induced temperature changes.

Figure 11 shows the nighttime evolution of the changes in the simulated temperature, TT_PBL and TT_ADV over the WFR from all three experiments (ALL, TUR and MOM). Consistent with what we have shown previously, the momentum sink component is responsible for the surface cooling signal whereas the TKE component contributes to the surface warming signal. Both components produce the warming around the hub-height levels and the cooling above it (Fig. 11a–c). Evidently, the nighttime evolution of TT_PBL (Fig. 11d–f) and TT_ADV (Fig. 11g–i) from all three experiments match well with the simulated temperature changes (Fig. 11a–c), which supports our idea that these two processes are very important to the WF-induced temperature changes. Note that the results from TT_ADV (Fig. 11g–i) display almost identical patterns as those from
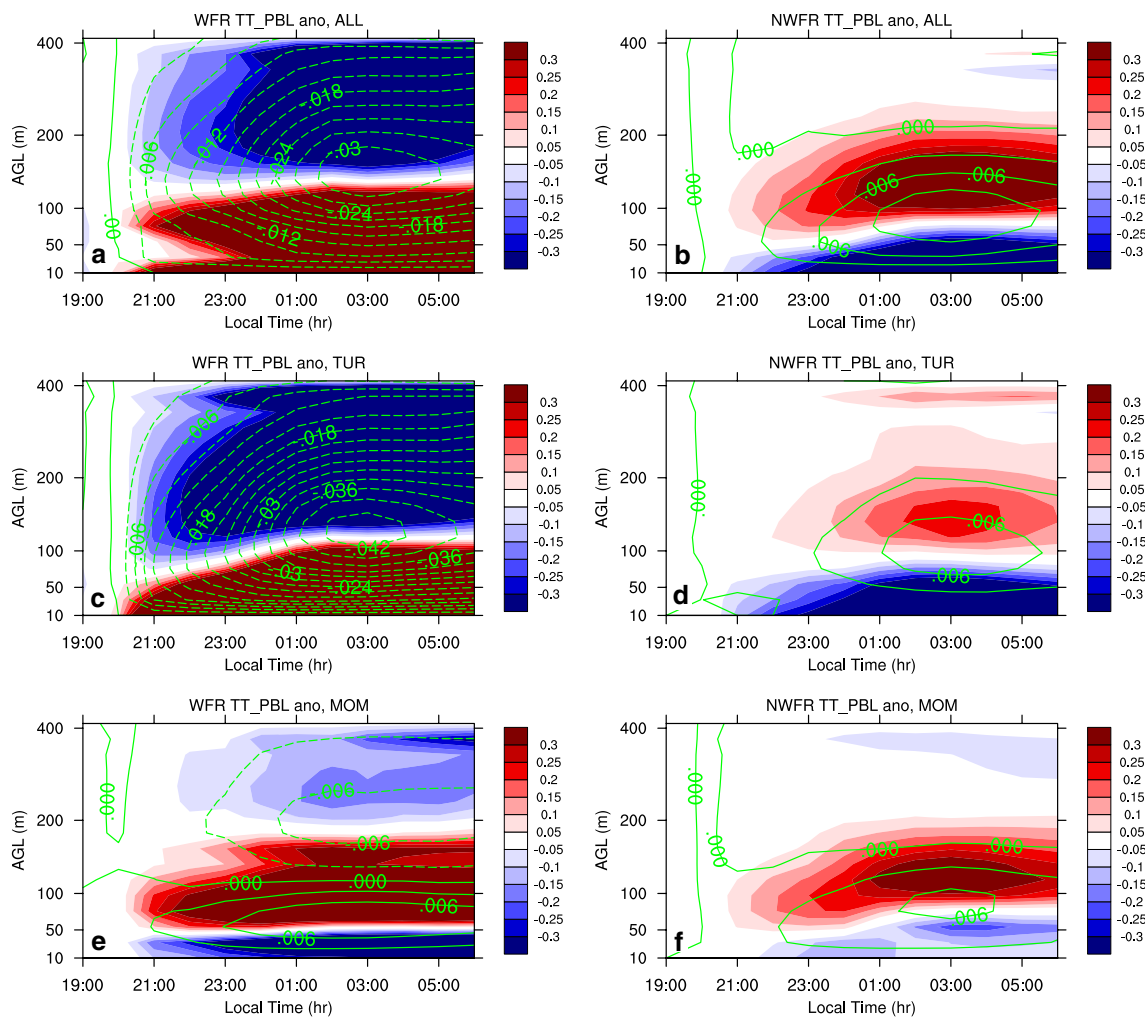
Fig. 8 Evaluation of TT_PBL (K h^{-1}) and $w'\theta'$ (K m s^{-1}) differences between simulations with and without the wind turbine parameterization averaged over the WFR **(a, c, e)** and NWFR **(b, d, f)** from all three experiments (ALL, TUR and MOM). The changes in TT_PBL are shaded in color contour whereas the changes in $w'\theta'$ are indicated as green contour lines. The WFR and NWFR are defined from the realistic WF configuration in Fig. 2a

TT_PBL (Fig. 11d–f) but the sign is reversed, indicating that the temperature changes induced from these two processes largely offset each other. Figure 12 shows the same figure as Fig. 11 but over the NWFR. Overall, the primary conclusions from the NWFR are very similar to these from the WFR. Note that the changes in TT_PBL from the TUR experiment (Fig. 12e) suggest cooling near the surface but warming around the hub-height levels, which is completely opposite to the simulated temperature changes (Fig. 12b). In this case, it is TT_ADV (Fig. 12h) that explains most of the simulated temperature responses. This strongly points out the important role of 3-D temperature advection to the WF-induced temperature changes, particularly over the downwind region.

Even though Figs. 11 and 12 indicate that the processes from the PBL scheme and temperature advection are very important to the simulated temperature changes, it is still not

a direct comparison because their units are different. To conduct a quantitative comparison, we compute the temperature tendency from the simulated temperature changes (TT_STC) and compare with that from TT_COMBINE. Figures 13 and 14 are the results over both the WFR and NWFR respectively. Overall, the changes in TT_STC and TT_COMBINE share many features such as, the near-surface warming signal from the TUR experiment, the near-surface cooling signal from the MOM experiment as well as the upper-layer cooling signal from both experiments. In addition, the changes in magnitude are very similar as well. However, there are still inconsistencies between the two terms, which we will discuss in more detail in the next section. Note that the pattern correspondence between TT_COMBINE and TT_STC is weak before 21:00 LT probably because the PBL is transitioning from daytime convective state to nighttime stable state (Fig. 6). Nevertheless, the results clearly indicate that
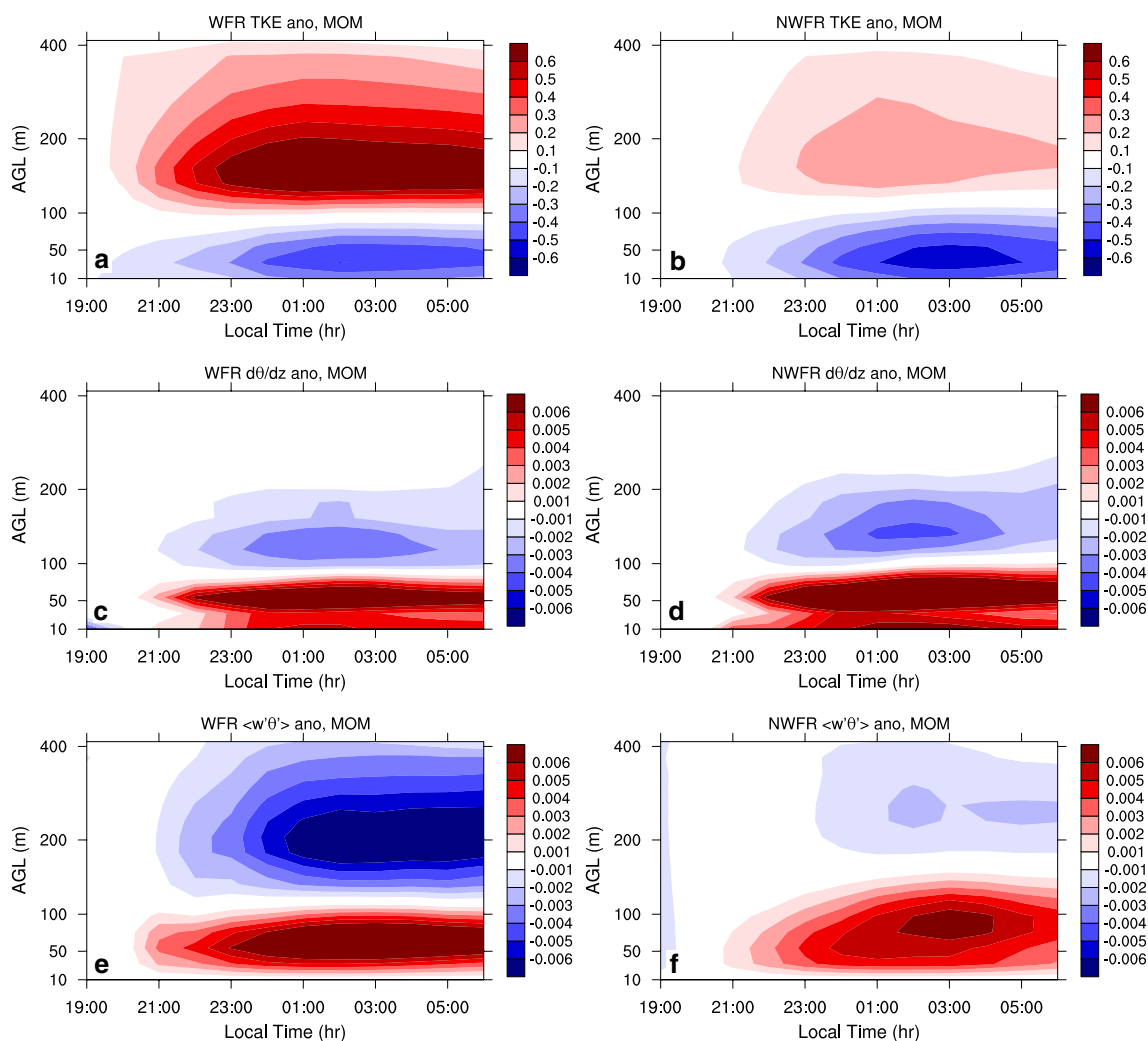
Fig. 9 Evaluation of TKE (m^2 s^{-2}), $d\theta/dz$ (K m^{-1}) and w$'\theta'$ (K m s^{-1}) differences between simulations with and without the wind turbine parameterization averaged over the WFR (**a, c, e**) and NWFR (**b, d, f**) from the MOM experiments

the PBL scheme and the 3-D temperature advection are the two critical physical processes responsible for the simulated temperature changes over both the WFR and NWFR.

4 Uncertainties

Zhou et al. (2013a, b) discussed the observational uncertainties associated with the MODIS LST data. Xia et al. (2017b) quantified the modeling uncertainties associate with the choice of surface layer schemes and land surface models, variations in topography, changes in vertical resolution, the threshold of clear-sky definition via various sensitivity tests, and validated wind statistics with limited SoDAR observations (Wilczak et al. 2014). These results point to some limitations of the current wind turbine parameterization, but such uncertainties have minor impacts on the robustness of

the simulated WF-induced surface warming signal in the WFR and the downwind cooling signal.

Next, we will focus on some new perspectives that are not addressed in the previous study. Although the general features of TT_COMBINE and TT_STC tend to agree with each other (Figs. 13, 14), there are still some discrepancies that need further examination. For example, TT_COMBINE indicates a positive temperature tendency near the surface between 03:00 LT and 06:00 LT over the WFR whereas the simulated warming signal starts to weaken after 03:00 LT. In addition, the upper layer (> 200 m) cooling signal is also not very well captured by TT_COMBINE over both the WFR and NWFR. An obvious reason for these discrepancies is that we only incorporate temperature tendencies from two processes (turbulent heat transport and temperature advection) to compare with the overall simulated temperature changes. Other physical (e.g., radiation, microphysics) and

Fig. 10 Areal mean vertical profiles of the wind speed between 19:00 LT and 06:00 LT from the CTR and MOM experiment: **a** averaged over the WFR defined in Fig. 2a, **b** averaged over the NWFR defined in Fig. 2a
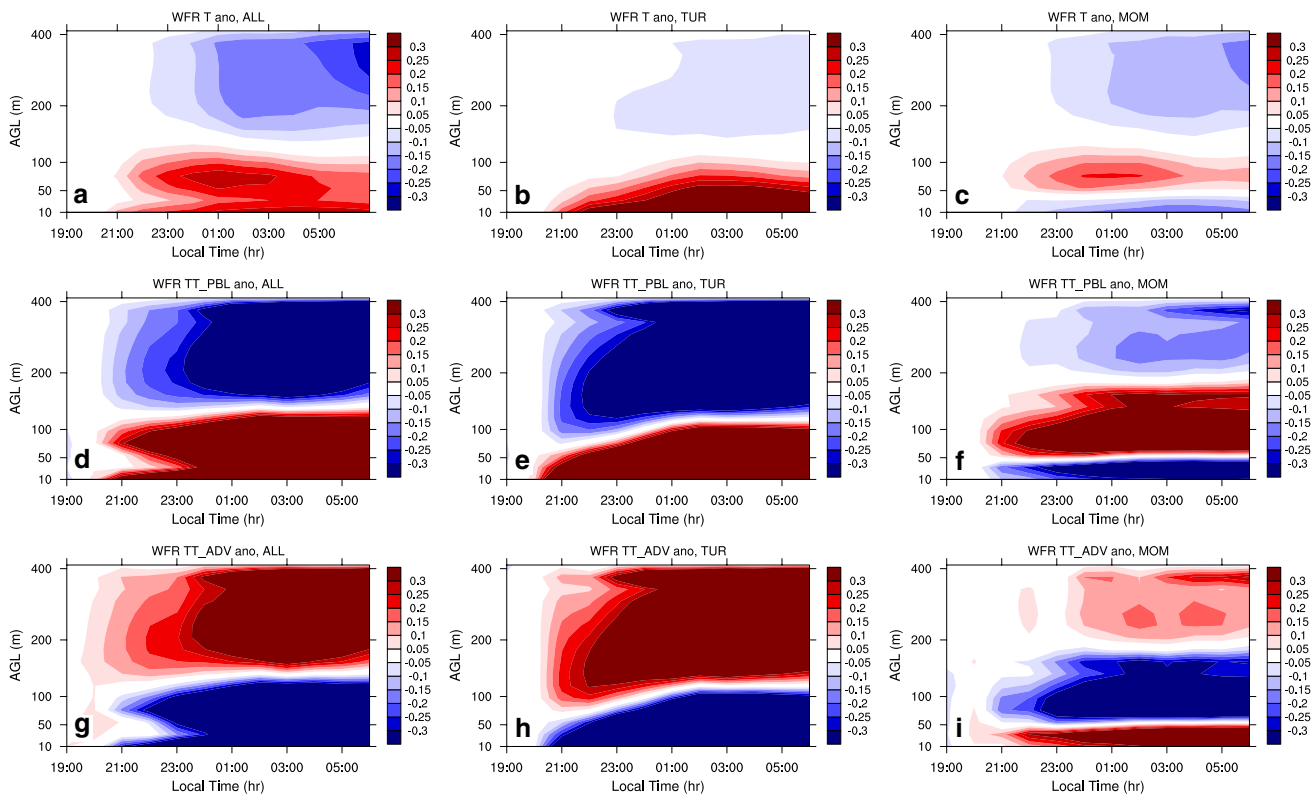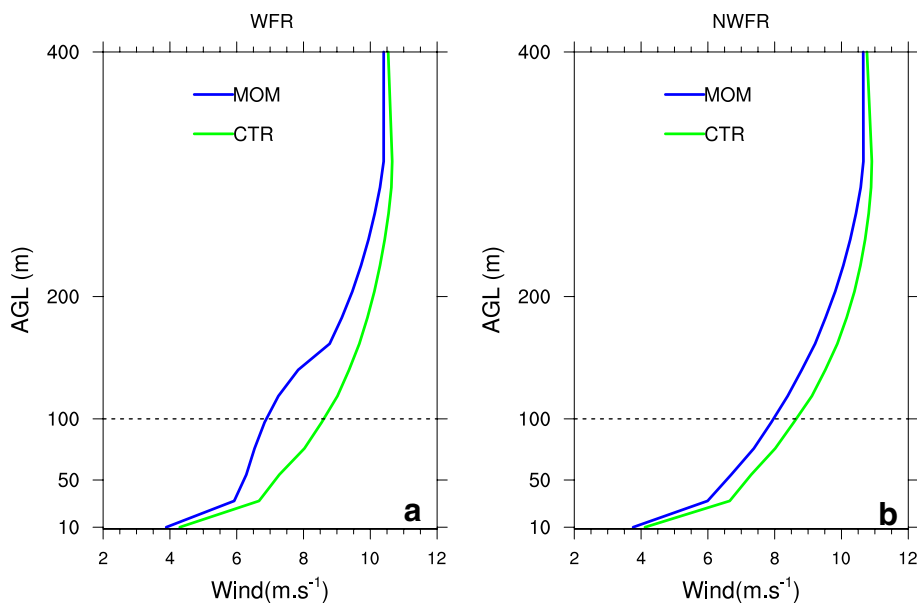

Fig. 11 Evolution of the simulated temperature (K), TT_PBL (K h^{-1}) and TT_ADV (K h^{-1}) differences between simulations with and without the wind turbine parameterization averaged over the WFR from 19:00 LT to 06:00 LT: **a–c** simulated temperature changes from the ALL, TUR and MOM respectively; **d–f** similar to **a–c** but for TT_PBL changes; **g–i** similar to **a–c** but for TT_ADV changes. The WFR is defined from the realistic WF configuration in Fig. 2a

dynamical processes (e.g., diffusion) might also be important. Note that we have examined the temperature tendency changes from radiation and diffusion schemes (Figure S3)

but their impacts are negligible as compared to TT_PBL and TT_ADV (Fig. 11). Another possible factor might be the nonlinear interaction between different processes simulated
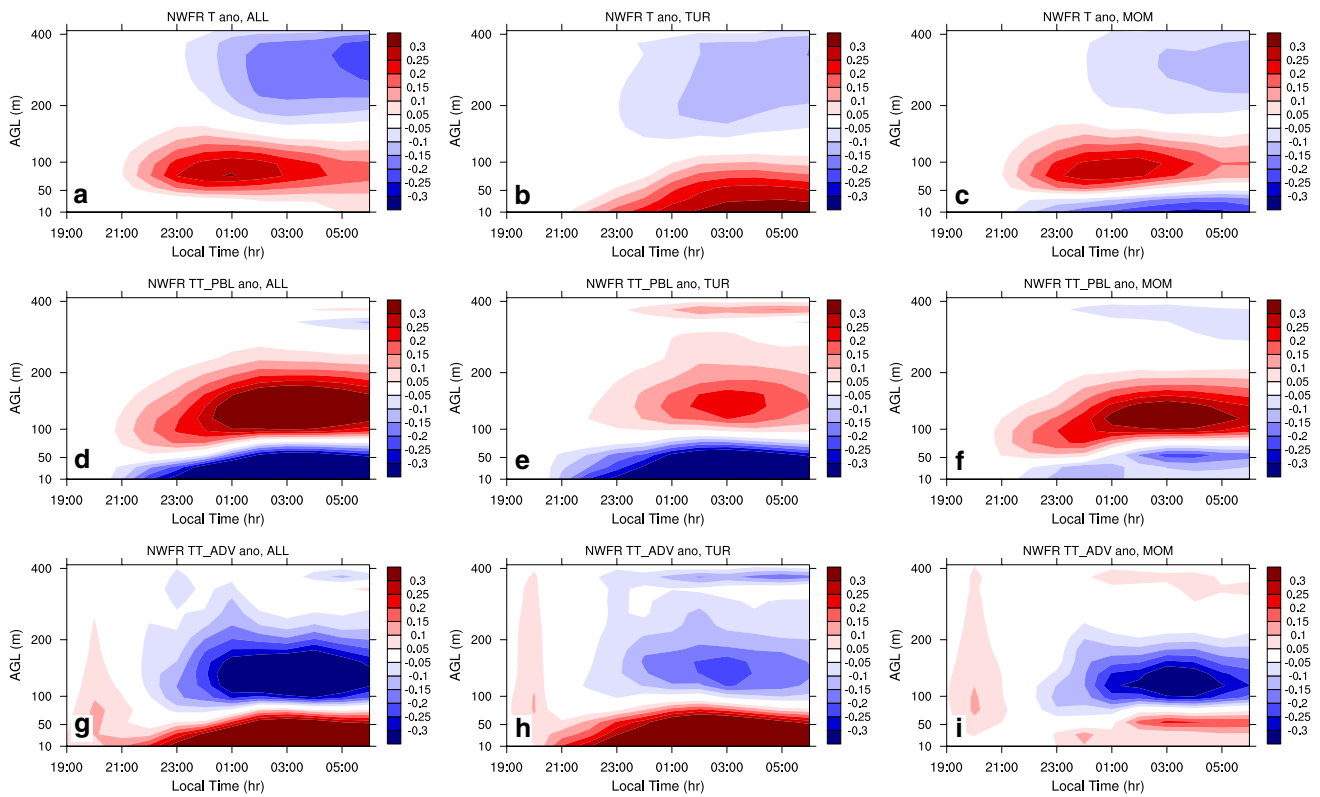
Fig. 12 Same as Fig. 11 but over the NWFR defined from the realistic WF configuration in Fig. 2a
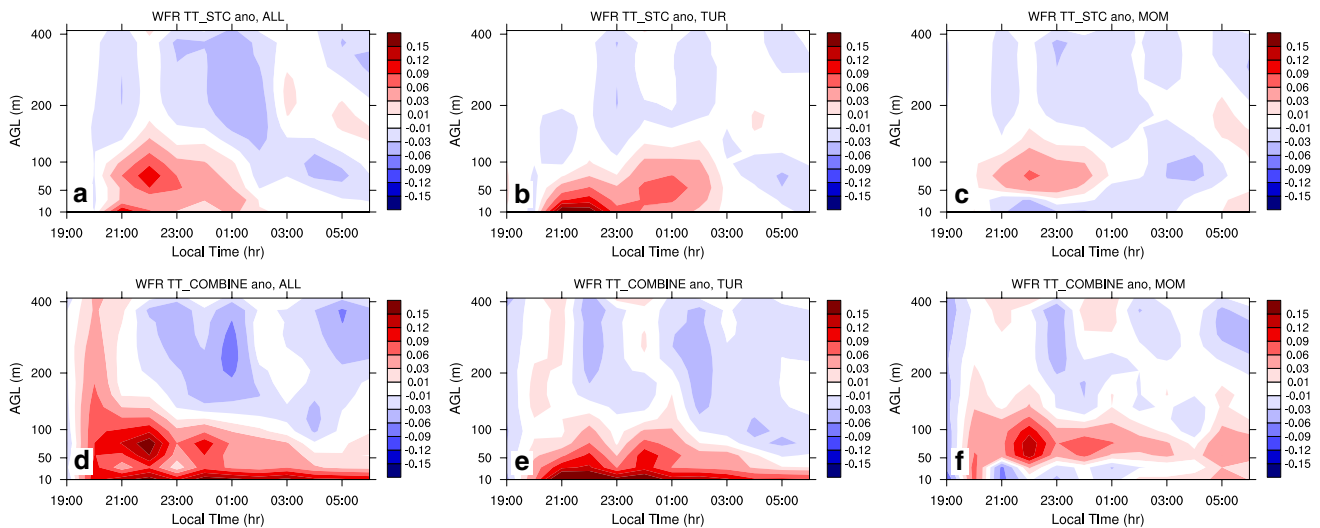

Fig. 13 Evolution of TT_STC (K h^{-1}) and TT_COMBINE (K h^{-1}) differences between simulations with and without the wind turbine parameterization averaged over the WFR from 19:00 LT to 06:00 LT: **a–c** TT_STC changes from the ALL, TUR and MOM respectively; **d–f** similar to **a–c** but for TT_COMBINE changes. WFR is defined from the realistic WF configuration in Fig. 2a

in the WRF model, which is a common problem for numerical studies. One good example is the linear summation of the changes of temperature from the TUR and MOM experiments are stronger than the results from the ALL experiment (Fig. 3; Tables 1, 2) due to the non-linear interactions

between the momentum and TKE equations in the MYNN PBL scheme.

Compared to Xia et al. (2017b), this paper only examines the month of July in 2011. However, both the wind speed and wind direction distribution during this month is qualitatively
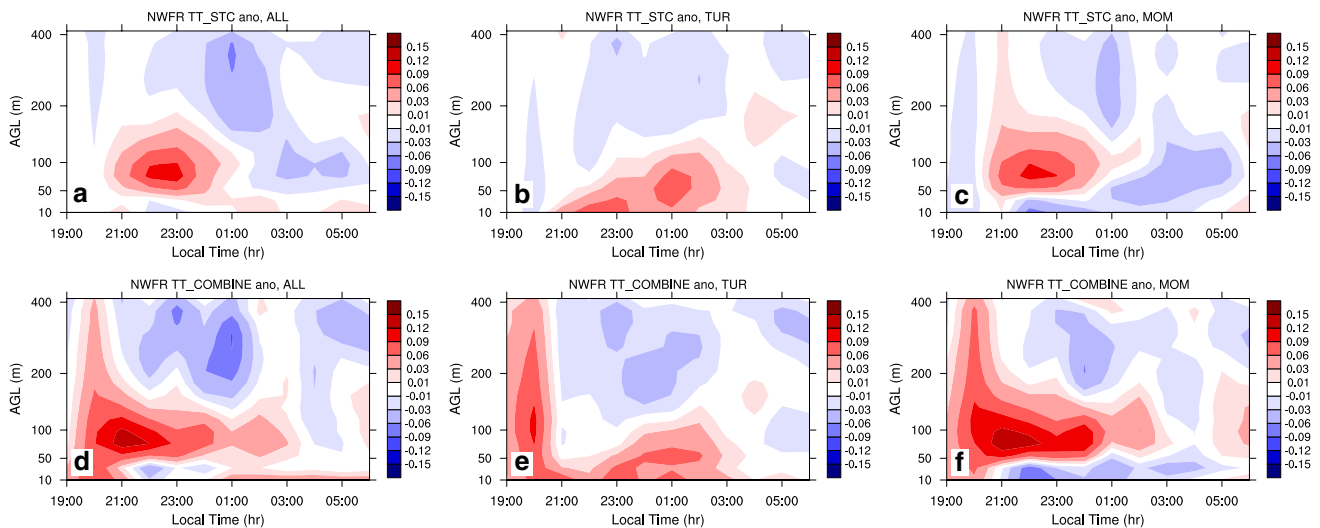
Fig. 14 Same as Fig. 13 but over the NWFR defined from the realistic WF configuration in Fig. 2a

similar to the multi-year average (Xia et al. 2017b), suggesting that the WTs are mostly working during the nighttime of the simulation period. Figure S4 illustrates the time series of simulated LST changes (22:00 LT–02:00 LT) averaged over the WFR and NWFR from the ALL, MOM and TUR experiments. The variability of the simulated temperature change signals is quite large. This is expected due to the changes in background weather conditions (i.e., wind and LST), which are high-frequency signals (Zhou et al. 2012; Xia et al. 2017b). However, the warming and cooling signals from the TUR and MOM are very consistent in the sign (with persistent positive and negative changes) throughout the 30-day period, suggesting that the effect of the WT parameterization is not ambiguous but consistent.

5 Conclusions

Using realistic initial and boundary conditions, Xia et al. (2017b) examined the WRF model's ability in simulating real-world WF impacts on LST. They found that the current WT parameterization can reproduce the observed nighttime warming signal over the WFs region, but with a smaller magnitude. However, the model also tends to produce a downwind cooling effect. This study furthers their research to uncover the spatiotemporal features of the simulated temperature changes and relevant physical processes. Specifically, two fundamental scientific questions are addressed: (i) what is the 3-D structure of near-surface temperatures within and around the WFs, and (ii) what are the main physical mechanisms responsible for the simulated WF-induced temperature changes? We conduct a series of WF simulations for the month of July 2011 and define two different

WF configurations to better illustrate the detailed evolution of the WF-induced temperature changes over both the WFR and NWFR.

Our modeling results indicate that: (i) large WFs can induce warming in WFR and cooling in NWFR, but have a minor or negligible net impact on regional surface temperature if averaging ΔLST over the two model domains of WFR and NWFR; (ii) the WF-induced changes in SH flux is the dominant surface forcing responsible for the simulated temperature changes, both over the WFR and NWFR; (iii) the WF-induced temperature changes are not only restricted to the surface but also can extend vertically above the hub-height level and horizontally into the downwind direction; (iv) the vertical divergence of heat flux from the PBL scheme and resolved 3-D temperature advection are the two most important physical processes behind the simulated temperature changes. At nighttime, the TKE component of the WT parameterization is responsible for the surface warming signal by bringing warm air down towards the surface through enhanced vertical mixing. The momentum sink component induces the surface cooling signal by reducing the wind speeds and by strengthening the near-surface thermal stratification through reducing the wind shear, which produce a less favorable background environment for turbulent heat fluxes to transport warmer air from aloft to the surface. Both components contribute to the simulated temperature changes (e.g., warming or cooling) above the surface.

Note that there is an interesting debate in WF parameterization, notably whether or not the added turbulence term in Fitch's scheme should be included. Jacobson and Archer (2012) and Volker et al. (2015) argue that this turbulence term is unnecessary while Vanderwende et al. (2015) indicates that it is important. Based on the present study

and Xia et al. (2017b), our results suggest that the turbulent component is needed as it is the critical component that is responsible for the warming signal over the WFR that has been confirmed by the previous satellite and field campaign studies. However, this is not a firm statement as there are discrepancies between our model simulation and observations. Thus, more WF validation studies are definitely needed.

Using the current WT parameterization in WRF, this research presents a fuller picture of the WF-induced temperature responses at nighttime over several large WFs and their downwind regions. However, most of the simulated temperature changes (e.g., surface cooling, hub-height warming and upper level cooling) have not been confirmed by any existed field observations because previous measurements are only taken at the immediate vicinity of WFs (Armstrong et al. 2014, 2016; Smith et al. 2013; Rajewski et al. 2013, 2014, 2016). As the simulated surface cooling signal has also not been observed by satellite observations, it is likely that the simulated cooling signal over the NWFR may result from model deficiencies in describing WF-atmosphere interaction and thus should be interpreted with caution. This calls for more comprehensive field campaigns to fully examine and understand the interactions of WFs and near-surface microclimate, which will be beneficial for improving the current WT parameterization as well as assessing real-world WF impacts on regional climate and agriculture as well.

References

Adams AS, Keith DW (2013) Are global wind power resources estimates overstated? Environ Res Lett. https://doi.org/10.1088/1748-9326/8/1/015021

Armstrong A, Waldron S, Whitaker J, Ostle NJ (2014) Wind farm and solar park effects on plant–soil carbon cycling: uncertain impacts of changes in ground-level microclimate. Glob Change Biol. https://doi.org/10.1111/gcb.12437

Armstrong A, Burton RR, Lee SE, Mobbs S, Ostle N, Smith V, Whitaker J (2016) Ground-level climate at a peatland wind farm in Scotland is affected by wind turbine operation. Environ Res Lett 11:044024

Baidya RS, Traiteur JJ (2010) Impacts of wind farms on surface air temperatures. Proc Nat Acad Sci. https://doi.org/10.1073/pnas.1000493107

Cervarich M, Baidya RS, Zhou L (2013) Spatiotemporal structure of wind farm-atmospheric boundary layer interactions. Energy Procedia 40:530–536

Chang R, Zhu R, Guo P (2016) A case study of land-surface-temperature impact from large-scale deployment of wind farms in China from Guazhou. Remote Sens. https://doi.org/10.3390/rs8100790

Fitch AC, Olson J, Lundquist J, Dudhia J, Gupta A, Michalakes J, Barstad I (2012) Local and mesoscale impacts of wind farms as parameterized in a mesoscale NWP model. Mon Weather Rev 204:3017–3038

Fitch AC, Lundquist JK, Olson JB (2013) Mesoscale influences of wind farms throughout a diurnal cycle. Mon Weather Rev 141(7):2173–2198

Harris RA, Zhou L, Xia G (2014) Satellite observations of wind farm impacts on nocturnal land surface temperature in Iowa. Remote Sens 6(12):12234–12246

Jacobson MZ, Archer CL (2012) Saturation wind power potential and its implications for wind energy. Proc Nat Acad Sci 109(39):15679–15684

Jimenez PA, Navarro J, Palomares AM, Dudhia J (2015) Mesoscale modeling of offshore wind turbine wakes at the wind farm resolving scale: a composite-based analysis with the Weather Research and Forecasting model over Horns Rev. Wind Energy 18(3):559–566

Lee JCY, Lundquist JK (2017) Observing and simulating wind-turbine wakes during the evening transition. Bound Layer Meteorol 163(3):449–474

Nakanishi M, Niino H (2009) Development of an improved turbulence closure model for the atmospheric boundary layer. J Meteorol Soc Jpn 87:895–912

Rajewski DA, Tackle ES, Lundquist JK, Oncley S, Prueger JH, Horst T, Rhodes M, Pfeiffer R, Hatfield JL, Spoth K, Doorenbos R (2013) Crop wind energy experiment (CWEX): observations of surface-layer, boundary layer, and mesoscale interactions with a wind farm. Bull Am Meteorol Soc 94:655–672

Rajewski DA, Takle ES, Lundquist JK, Prueger JH, Pfeiffer RL, Hatfield JL, Doorenbos RK (2014) Changes in fluxes of heat, H_2O, and CO_2 caused by a large wind farm. Agric For Meteorol 194:175–187

Rajewski DA, Takle ES, Prueger JH, Doorenbos RK (2016) Toward understanding the physical link between turbines and microclimate impacts from in situ measurements in a large wind farm. J Geophys Res Atmos 121(22):13392–13414

Skamarock WC, Klemp JB (2008) A time-split nonhydrostatic atmospheric model for weather research and forecasting applications. J Comput Phys 227:3465–3485

Skamarock WC et al (2008) A description of the advanced research WRF version 3. Tech. Rep. NCAR/TN-475 + STR

Slawsky LM, Zhou L, Baidya SR, Xia G, Vuille M, Harris RA (2015) Observed thermal impacts of wind farms over northern illinois. Remote Sens 15(7):14981–15005

Smith CR, Barthelmie RJ, Pryor SC (2013) In situ observations of the influence of a large onshore wind farm on near-surface temperature, turbulence intensity and wind speed profiles. Environ Res Lett 8:034006

Sun H, Luo Y, Zhao Z, Chang R (2018) The impacts of Chinese wind farms on climate. J Geophys Res Atmos 123:5177–5187. https://doi.org/10.1029/2017JD028028

Tang B, Wu D, Zhao X, Zhou T, Zhao W, Wei H (2017) The observed impacts of wind farms on local vegetation growth in Northern China. Remote Sens 9(4):332

Vanderwende B, Lundquist JK, Rhodes ME, Takle GS, Purdy SI (2015) Observing and simulating the summertime low-level jet in central Iowa. Mon Weather Rev 143:2319–2336

Volker PJH, Badger J, Hahmann AN, Ott S (2015) The explicit wake parameterization v1.0: a wind farm parameterization in the mesoscale model WRF. Geosci Model Dev 8(11):3715–3731

Wilczak J, Finley C, Freedman J, Cline J, Bianco L, Olson J, Djalalova I, Sheridan L, Ahlstrom M, Manobianco J, Zack J, Carley J, Benjamin S, Marquis M (2014) The wind forecast improvement project (WFIP): a public-private partnership addressing wind energy forecast needs. Bull Am Meteorol Soc. https://doi.org/10.1175/BAMS-D-14-00107.1

Xia G, Zhou L (2017a) Detecting wind farm impacts on local vegetation growth in Texas and Illinois using MODIS vegetation greenness measurements. Remote Sens 9:698

Xia G, Zhou L, Freedman JM, Roy SB, Harris RA, Cervarich MC (2016) A case study of effects of atmospheric boundary layer turbulence, wind speed, and stability on wind farm induced temperature changes using observations from a field campaign. Clim Dyn 46:1–18

Xia G, Cervarich M, Baidya SB, Zhou L, Minder J, Freedam JM, Jiménez PA (2017b) Simulating impacts of real-world wind farms on land surface temperature using WRF model: validation with MODIS observations. Mon Weather Rev 145:4813–4836

Zhou L, Dickinson RE, Ogawa K, Tian Y, Jin M, Schmugge T, Tsvetsinskaya E (2003a) Relations between albedos and emissivities from MODIS and ASTER data over North African desert. Geophys Res Lett 30(20):2026

Zhou L, Dickinson RE, Tian Y, Jin M, Ogawa K, Yu H, Schmugge T (2003b) A sensitivity study of climate and energy balance simulations with use of satellite derived emissivity data over the northern Africa and the Arabian peninsula. J Geophys Res 108(D24):4795. https://doi.org/10.1029/2003JD004083

Zhou L, Tian Y, Baidya RS, Thorncroft C, Bosart LF, Hu Y (2012) Impacts of wind farms on land surface temperature. Nat Clim Change 2(7):539–543

Zhou L, Tian Y, Baidya RS, Dai Y, Chen H (2013a) Diurnal and seasonal variations of wind farm impacts on land surface temperature over western Texas. Clim Dyn 41:307–326

Zhou L, Tian Y, Chen H, Dai Y, Harris RA (2013b) Effects of topography on assessing wind farm impacts using MODIS data. Earth Interact 17(13):1–18